

Study of star formation in RCW 106 using far infrared observations

A.D. Karnik, S.K. Ghosh, T.N. Rengarajan and R.P. Verma[★]

Tata Institute of Fundamental Research, Homi Bhabha Road, Mumbai (Bombay) 400 005, India

2001 April 4

ABSTRACT

High resolution far-infrared observations of a large area of the star forming complex RCW 106 obtained using the TIFR 1m balloon-borne telescope are presented. Intensity maps have been obtained simultaneously in two bands centred around 150 and 210 μm . Intensity maps have also been obtained at the four *IRAS* bands using HIRES processed *IRAS* data. From the 150 and 210 μm maps, reliable maps of dust temperature and optical depth have been generated. The star formation in this complex has occurred in five linear sub-clumps. Using the map at 210 μm , which has a spatial resolution superior to that of the *IRAS* at 100 μm , 23 sources have been identified. The spectral energy distribution (SED) and luminosity of these sources have been determined using the associations with the *IRAS* maps. Luminosity distribution of these sources has been obtained. Assuming these embedded sources to be ZAMS stars and using the mass-luminosity relation for these, the power law slope of the initial mass function is found to be -1.73 ± 0.5 . This index for this very young complex is about the same as that for more evolved complexes and clusters. Radiation transfer calculations in spherically symmetric geometry have been undertaken to fit the SEDs of 13 sources with fluxes in both the TIFR and the *IRAS* bands. From this, the r^{-2} density distribution in the envelopes is ruled out. Finally, a correlation is seen between the luminosity of embedded sources and the computed dust masses of the envelopes.

Key words:

ISM : clouds – dust – stars : formation

[★] Send all correspondences to : vermarp@tifr.res.in

1 INTRODUCTION

Far-Infrared (FIR) observations provide an important tool to study formation of high mass stars, especially at a very early stage of their formation when they are deeply embedded in their parent clouds. The TIFR group has been active in observing in the FIR, especially at trans-*IRAS* wavelengths, using the TIFR 1m balloon-borne telescope (Ghosh et al. 1988; Ghosh et al. 1989a; Ghosh et al. 1989b; Ghosh et al. 1990; Ghosh et al. 2000; Verma et al. 1994; Mookerjee et al. 1999; Mookerjee et al. 2000). Taking advantage of our location, we have been mapping several star forming complexes in the southern hemisphere, not easily accessible from the higher latitudes of northern hemisphere. Balloon-borne telescope is also efficient in mapping a large area with moderate sensitivity. In this paper we describe our study of high mass star formation in RCW 106, a large southern star forming complex. This complex, harbouring a score or more of high mass stars, provides us an opportunity to study the mass function of stars at a very early stage and the physical conditions of their envelopes. This is aided by our simultaneous mapping at 150 and 210 μm with a high spatial resolution of $\sim 1'$ enabling us to resolve more sources than the *IRAS* at 100 μm .

RCW 106 is an optically visible H II region in the southern Galactic plane. The distance of this H II region is 3.6 kpc (Lockman 1979). It was discovered by Rodgers, Campbell & Whiteoak (1960) while they were surveying the southern milky way in $\text{H}\alpha$ line emission. Radio continuum emission towards this region has been mapped by Shaver & Goss (1970a) and Goss & Shaver (1970) at 408 MHz and 5000 MHz. Interferometric observations of a part of the region are available at 1415 MHz (Retallack & Goss, 1980), 1420 MHz (Forster et al. 1987), 6.67 GHz and 8.64 GHz (Walsh et al. 1998). The associated molecular cloud was detected by Gillespie et al. (1977) during their observations of southern Galactic H II regions in the $J = 1-0$ transition of CO. Similarly, interstellar molecules like OH (Caswell & Haynes 1975), H_2O (Kaufmann et al. 1977), NH_3 (Batchelor et al. 1977), CS (Gardner & Whiteoak 1978) and H_2CO (Gardner & Whiteoak 1984) were detected towards this region indicating extremely dense molecular material. Several maser sources in the lines of H_2O (Batchelor et al. 1980; Braz & Scalise 1982; Braz et al. 1989; Scalise, Rodriguez & Mendoza-Torres 1989), OH (Caswell, Haynes & Goss 1980) and methanol (Macleod & Gaylard 1992; Schutte et al. 1993; Caswell et al. 1995; van der Walt, Gaylard & Macleod 1995; van der Walt et al. 1996; Ellingsen et al. 1996; Macleod et al. 1998) have been detected towards this complex

in independent surveys and observations towards selected *IRAS* sources. All these suggest ongoing high mass star formation in the region.

In the next section we describe the observations and details of the photometer employed. In Sec. 3 the intensity maps in the two bands and the derived maps of dust temperature and optical depth are presented. Intensity maps from HIREs processed *IRAS* observations are also presented in the four *IRAS* bands. Sources extracted from these maps and the spectral energy distribution (SED) derived from our and *IRAS* observations as well as the comparison of FIR sources with the radio continuum sources are also presented. Sec. 4 presents a discussion of the FIR luminosity distribution and the initial mass function (IMF) derived from this. Sec. 5 describes the physical properties of the envelopes of selected sources based on radiation transfer modelling. The results are summarised in the last section. More details of this study can be found in the PhD thesis of Karnik (Karnik 2000).

2 OBSERVATIONS

2.1 Balloon-borne FIR observations

The observations were carried out on February 20, 1994 using a two band array photometer in the focal plane of the TIFR 1m balloon-borne telescope which was launched from the TIFR Balloon Facility, Hyderabad, India. Details of the telescope and observing procedures have been described by Ghosh et al. (1988). The photometer used has been described by Verma, Rengarajan & Ghosh (1993). It consists of a pair of compact arrays each having 2×3 silicon bolometers cooled to 0.3 K by liquid ^3He . The field of view of each detector was $1'.6$. The sky was chopped along the cross elevation axis with a throw of $4'.2$. Two bands centred around 150 and 210 μm were obtained by splitting the incoming beam using a cooled dichroic filter and other band limiting filters. The sky viewed in the two bands was almost identical. Jupiter was used for flux calibration as well as for obtaining the point spread function (PSF). A large area of about 1.2° of RCW 106 complex was mapped in five overlapping rasters.

All six detectors of each band were independently calibrated for their responsivity by using in situ measurements of Jupiter. The telescope aspects corresponding to different detectors of each band were reduced to a reference detector using the known relative positions in the focal plane. The responsivity corrected signals (during the mapping observations of the target source), from all detectors of the same band were then gridded into a two dimensional

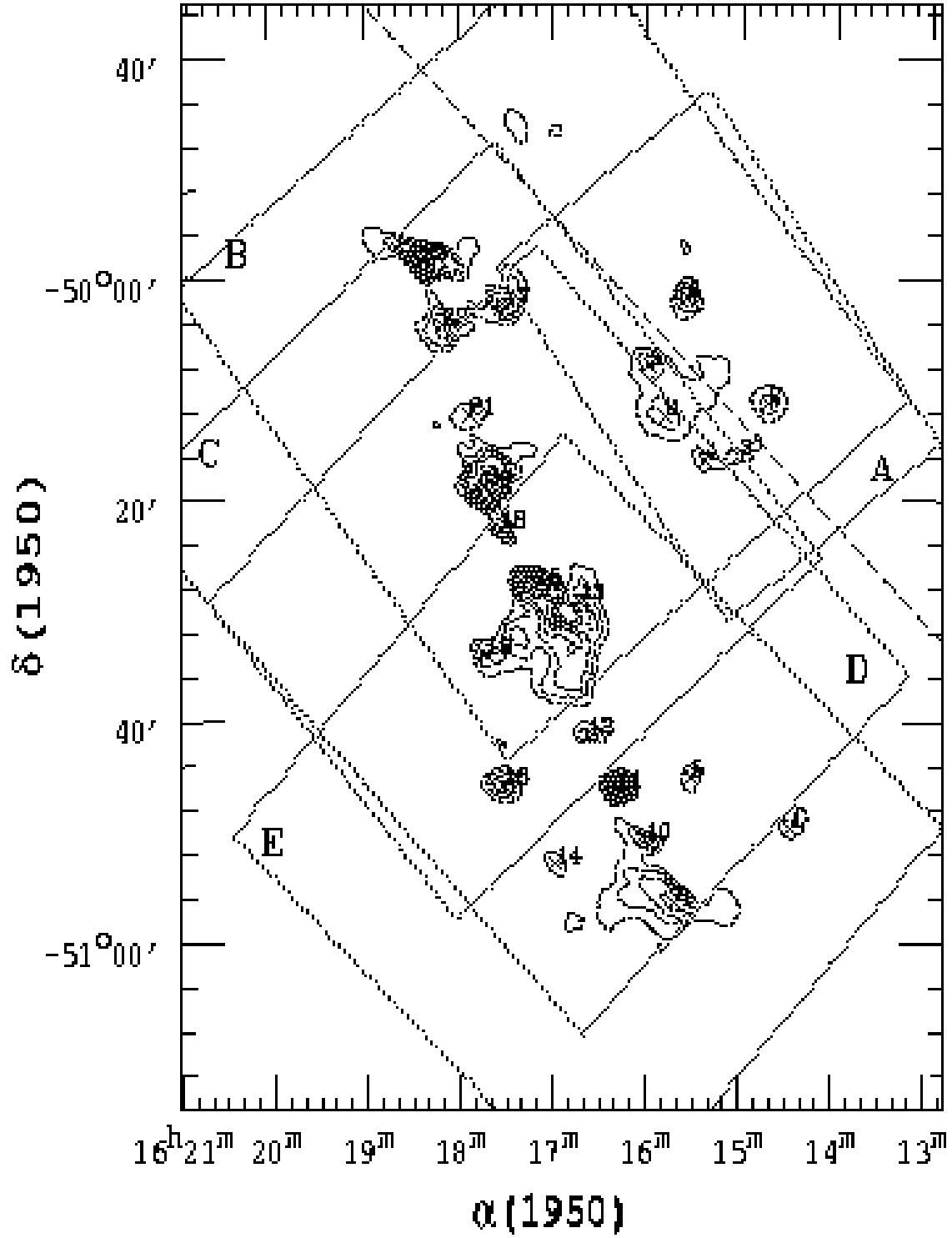


Figure 1. The map of RCW 106 region at $210\ \mu\text{m}$. Contour levels are drawn at 1, 2.5, 5, 10, 20, 30, 50, 70 and 90 percent of peak intensity ($4375\ \text{Jy}/\square'$). The rectangular boxes show the approximate area covered by each of the individual raster scans A, B, C, D and E respectively. The dashed line shows the position of the Galactic plane. The crosses show positions of the detected sources.

sky matrix (elevation \times cross elevation; cell size of $0'.3 \times 0'.3$). This signal matrix was deconvolved using a procedure based on maximum entropy method (MEM; see Ghosh et al. 1988 for details). The FWHMs of the deconvolved beam for Jupiter were found to be $1' \times 1'.3$ (elevation \times cross elevation) for both bands.

Since our wavelength bands are broad, the flux density estimated from the observed signal is a function of the incident spectrum. Following the *IRAS* convention we present flux densities for a $\nu f_\nu = \text{constant}$ spectrum. When computing flux density for other spectral shapes a colour correction is applied such that $f_\nu(\text{actual}) = f_\nu(\text{quoted})/K$. For a gray body spectrum with emissivity $\epsilon \propto \lambda^{-1}$ the K factor at $150 \mu\text{m}$ varies from 0.85 to 0.57 as the temperature is varied from 20 K to 60 K; at $210 \mu\text{m}$ the variation is from 0.84 to 0.85. For an emissivity $\epsilon \propto \lambda^{-2}$ the corresponding values are 0.7 to 0.52 for the $150 \mu\text{m}$ band and 0.81 to 0.87 for the $210 \mu\text{m}$ band.

2.2 Pointing accuracy

The absolute pointing accuracy was determined in two different ways. (i) An optical photometer (with a photomultiplier tube as detector) at the cassegrain focal plane of the telescope always views a region of the sky neighbouring the FIR field (Naik et al. 2000). The sky chopped signals obtained from this photometer during the FIR scans across the target source were also MEM deconvolved to generate optical intensity maps of the scanned region. The stars detected in these maps have been used to quantify absolute aspects of our maps. Using 17 well identified and isolated optical stars, the mean deviation and rms were found to be $0'.2$ and $0'.7$ respectively along RA and $0'.06$ and $0'.68$ along the Dec axis. (ii) A similar exercise was carried out using the coordinates of six well isolated FIR sources in the *IRAS* as well as the TIFR maps. The rms deviations along RA and Dec axes were found to be $0'.45$ and $0'.2$ respectively. It may be mentioned that the FIR signal matrix has a much higher filling factor as compared to the optical signal matrix generated using only a single detector. Thus, our absolute pointing over an area as large as 1.2° observed over an hour is better than $0'.5$.

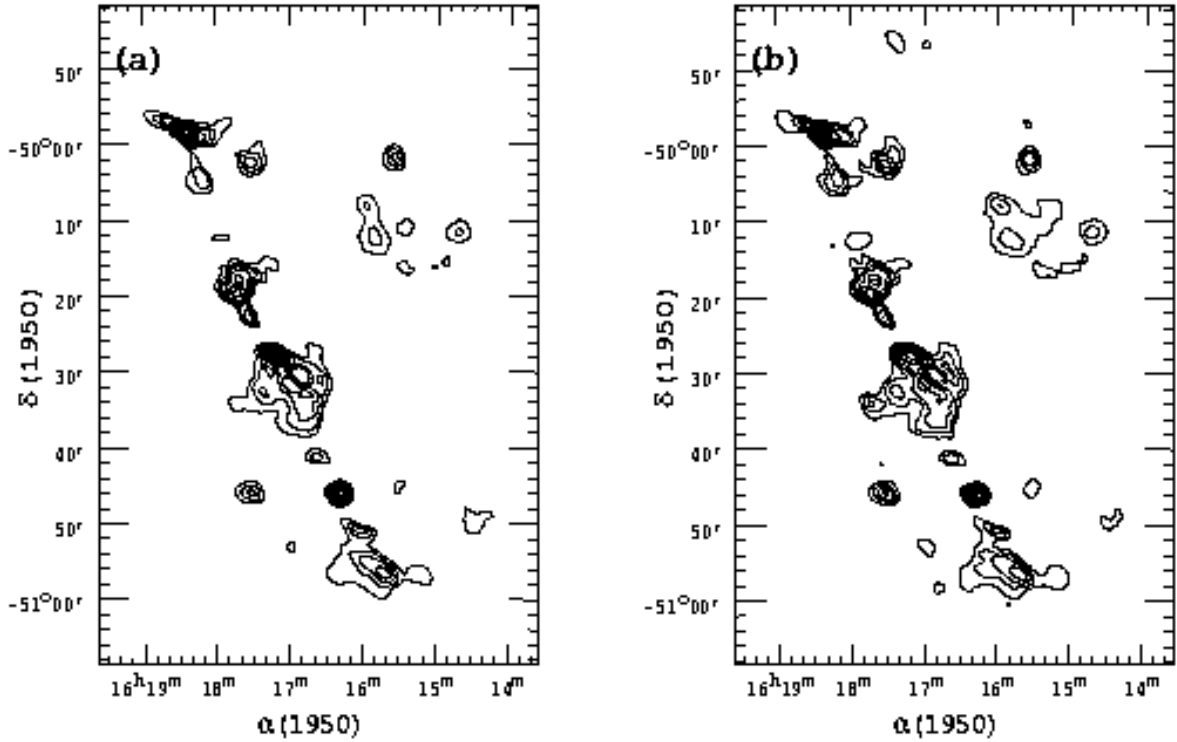


Figure 2. TIFR maps of RCW 106 region for (a) 150 & (b) 210 μm . Contour levels are drawn at 1, 2.5, 5, 10, 20, 30, 50, 70 and 90 percent of peak intensity 9728 and 4375 Jy / \square' at 150 and 210 μm respectively.

2.3 IRAS-HIRES maps

The HIRES maps processed from the *IRAS* data of RCW 106 region were obtained from the Infrared Processing and Analysis Center (IPAC[†], Caltech). These maps were processed using the maximum correlation method (MCM, Aumann, Fowler & Melnyk 1990). The resolution enhancement results in elliptical beams with FWHMs of $1'.0 \times 0'.45$, $0'.95 \times 0'.45$, $1'.3 \times 0'.7$, and $1'.9 \times 1'.3$ at 12, 25, 60 and 100 μm respectively. The position angle of the major axis of the beam is 100° . The overall variation in the beam size in different regions of the map is about 15%.

3 RESULTS

3.1 Intensity maps

Fig. 1 shows an enlarged intensity map at 210 μm obtained from our observations combining all the five rasters. The boundaries of individual raster areas are also shown. The long dashed

[†] IPAC is funded by NASA as part of the part of the *IRAS* extended mission program under contract to JPL.

line shows the position of the Galactic plane. In Fig. 2a and 2b we show the intensity maps at $150\ \mu\text{m}$ and $210\ \mu\text{m}$. The peak flux densities at 150 and $210\ \mu\text{m}$ are 9728 and $4375\ \text{Jy}/\square^\circ$ respectively while the noise is found to be 16 and $9\ \text{Jy}/\square^\circ$. The lowest contour level shown is 1% of the peak and is several times the noise. From the figures it is seen that the star formation in RCW 106 is along a narrow ridge roughly parallel to the Galactic plane. It is also seen that the FIR emission is subdivided into five collinear sub complexes.

Figs. 3a–d show the *IRAS* HIRES intensity maps at 12 , 25 , 60 and $100\ \mu\text{m}$. Once again the lowest contour level shown is 1% of the peak. The *IRAS* maps, especially at 60 and $100\ \mu\text{m}$ are morphologically similar to our maps. However, we resolve more sources as compared to the *IRAS*. The FIR maps are also very similar to the radio continuum maps of Goss & Shaver (1970) and Shaver & Goss (1970a).

3.2 Maps of temperature and optical depth

Far-infrared and sub-millimeter observations can be effectively used to obtain column densities of the region from the optical depth at these wavelengths (Hildebrand 1983). Recent studies using *IRAS* data at 60 and $100\ \mu\text{m}$ have shown that the $100\ \mu\text{m}$ optical depth correlates well with other column density indicators namely CO and visual extinction (Langer et al. 1989; Jarrett, Dickman & Herbst 1989). Since we have simultaneous observations in two trans-*IRAS* wavelengths with almost identical FOV, we make use of these maps to derive reliable maps of both the temperature and optical depth. Our longer wavelength coverage also makes our data more sensitive to colder dust (temperature down to about $15\ \text{K}$) as compared to the *IRAS* coverage. The intensity maps were smoothed by taking average within a box of 0.9×0.9 size and these were, in turn, used to obtain maps of temperature and optical depth. To derive the temperature, we assume an emissivity dependence $\epsilon \propto \lambda^{-2}$. These are shown in Fig. 4.

The temperature map shows a lot of structure and several high temperature regions near the cloud boundaries. These regions are, most probably, sites of H II blisters where the dust is heated by radiation from young stars close to the boundary. The optical depth map is morphologically similar to the intensity maps and the peaks in the two coincide indicating presence of high densities near the embedded sources.

Assuming a homogeneous mixture of silicate ($\rho = 3.3\ \text{g}/\text{cm}^{-3}$) and graphite ($\rho = 2.26\ \text{g}/\text{cm}^{-3}$) dust grains with a power law size distribution (index = -3.5) as given by Mathis,

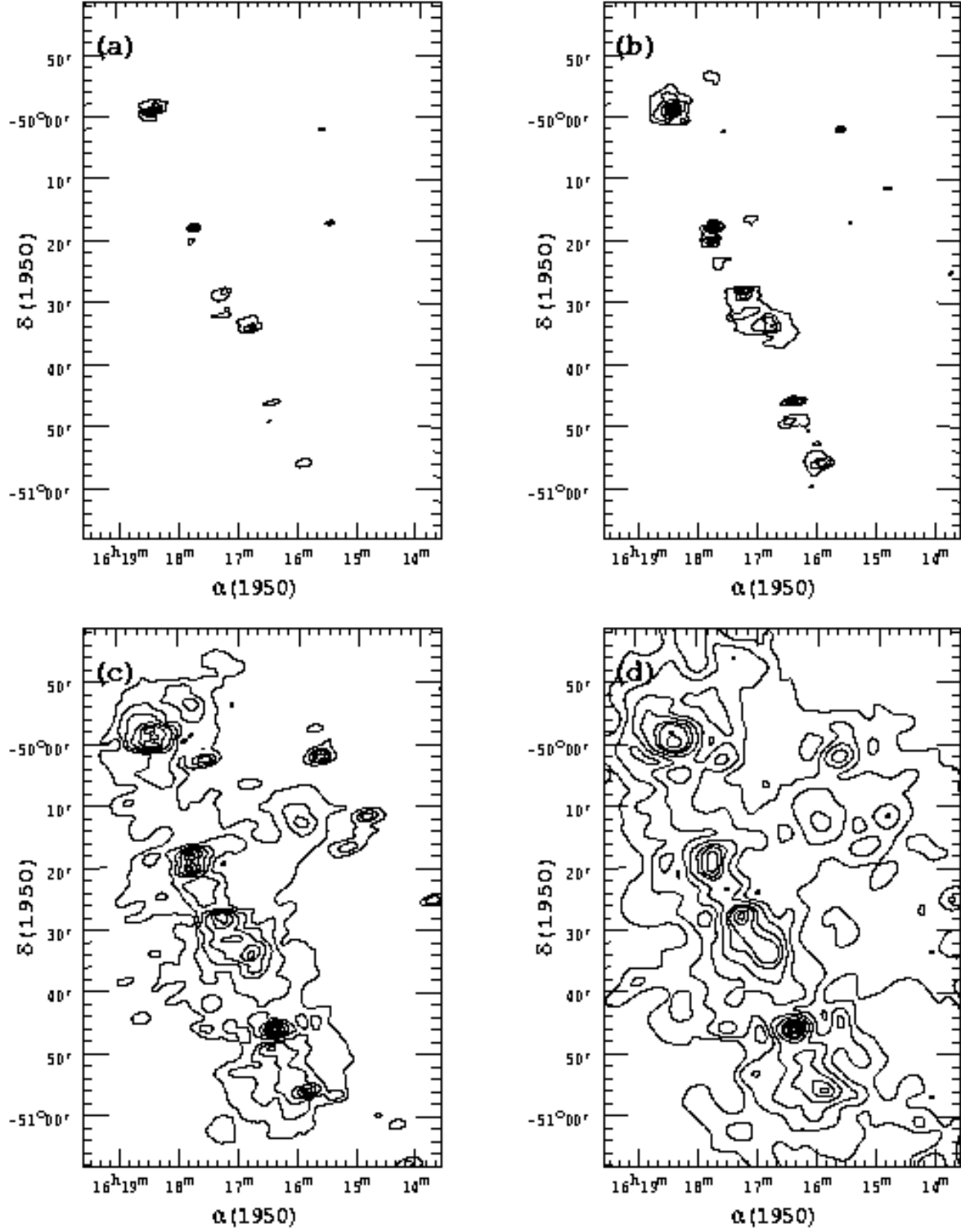


Figure 3. HIRES processed *IRAS* maps of RCW 106 region at (a) 12, (b) 25, (c) 60 and (d) 100 μm . Contour levels are drawn at 1, 2.5, 5, 10, 20, 30, 50, 70 and 90 percent of peak intensity 4875, 8455, 7947 and 4884 Jy/\square' for 12, 25, 60 and 100 μm respectively.

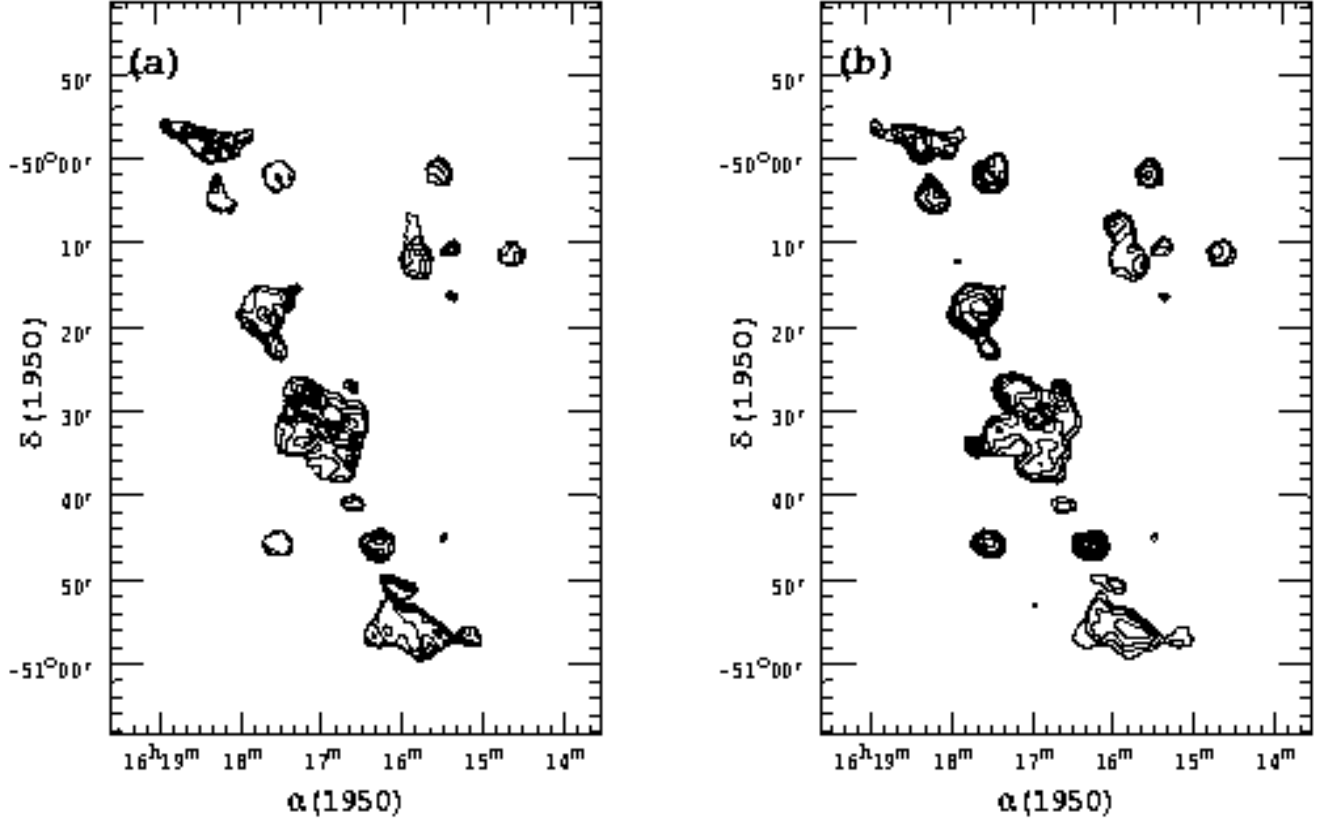


Figure 4. The maps of RCW 106 region for (a) Temperature ($T_{150/210}$) and (b) optical depth at $210\ \mu\text{m}$. The dust grain emissivity is assumed to be $\propto \nu^2$. Contours for temperature are plotted at 20, 24, 28, 32, 36, 40 and 44 K. Contours for optical depth are plotted at 1, 2.5, 5, 10, 20, 30, 50, 70, and 90 percent of peak optical depth of 0.10 .

Rumpl & Nordsieck (1977) and using the absorption efficiencies as per Laor & Draine (1993), we estimate the total dust mass of the complex to be equal to $1800\ M_{\odot}$. If one takes the gas to dust ratio to be 100, then the total mass of the cloud is $1.8 \times 10^5\ M_{\odot}$. This value is typical for a GMC of size of 70 pc in the Galactic plane. However it may be noted that this estimate of cloud mass may be an underestimate, because due to chopping, low gradient diffuse flux is missed in our observations (see next subsection).

3.3 Embedded sources

Flux calibrated maps (Figs. 2a and 2b) were processed to extract discrete sources and to obtain their flux densities. The HIRES processed maps of the *IRAS* survey data at 12, 25, 60 and $100\ \mu\text{m}$ were also used to supplement our observations. For all six bands (four *IRAS* and two of TIFR) the following procedure was adopted to extract sources. For each pixel in the image map, if the pixel value was greater than or equal to a specified threshold then the maximum pixel value within a box of size 5×5 pixels around this pixel was obtained. If the

pixel value was equal to this maximum, the position was assumed to be the peak position for a source and its centroid position was determined using the IRAF software. A total of 23 sources were thus found at 210 μm . More details can be found in Karnik (2000).

The associations of the above sources with sources in other maps viz. , 150 μm map of TIFR and the *IRAS* maps at 12, 25, 60 and 100 μm were searched for, demanding a centroid separation of less than 1'.0 at 150 μm and 1'.5 at other wavelengths. All 23 sources are detected at 150 μm . Eighteen of the 23 sources have *IRAS* associations with detection in two or more bands. We have five sources that are detected only in our maps. This is due to the superior resolution of our maps resulting from the smaller FOV. The flux densities of sources detected in each band were obtained using the numerical aperture photometry and an aperture value of 3' diameter; the sky background was evaluated as mode value within an annulus of 0'.5 width at radius of 4' and subtracted from each pixel before obtaining the aperture sum. The flux densities obtained at 150 and 210 μm bands were colour corrected assuming a gray body spectrum with emissivity $\propto \lambda^{-2}$, and a temperature corresponding to the ratio of fluxes in the two bands. The *IRAS* flux densities were colour corrected assuming a power law type of flux density distribution between two neighbouring bands. The overall errors on the total flux densities including calibration errors are about 15–20%. The colour corrected flux densities along with the source positions in the 210 μm map are presented in Table 1. The SED of each source was constructed using these tabulated values. The luminosities of the sources were derived by integrating the SED and assuming a distance of 3.6 kpc (Lockman 1979). Out of band correction based on the $T(150/210)$ was also made. For the five sources which were detected only in our maps the total flux was estimated from the temperature given by the ratio of flux densities and assuming $\epsilon \propto \lambda^{-2}$. For source S23, *IRAS* signals were saturated at 60 and 100 μm . We, therefore, estimated these by extrapolation from the 150 and 210 μm flux densities. The computed luminosities for all the sources are also shown in Table 1.

We estimate the diffuse emission in the complex by subtracting the sum of flux densities of the extracted sources from the total flux density of the map down to 1% contour level. We find the diffuse fraction to be 81%, 84%, 19% and 27% at 60, 100, 150 and 210 μm respectively. In contrast to the *IRAS*, our chopped observations are less sensitive to low gradient diffuse flux. The fraction of diffuse flux obtained using chopped observations of RCW 106 complex may be compared with values obtained for other regions using similar

Table 1. Positions at 210 μm and other properties of detected sources

| Source | R.A.* (1950) | DEC* (1950) | IRAS PSC | Flux Density in Jy [†] | | | | | | Lum. $10^3 L_\odot$ | IRE [‡] |
|--------|-----------------|----------------|------------|---------------------------------|------------------|------------------|-------------------|-------------------|-------------------|------------------------|------------------------|
| | | | | 12 μm | 25 μm | 60 μm | 100 μm | 150 μm | 210 μm | | |
| S1 | 16 14 27.6 | -50 49 40 | — | — | — | — | — | 872 | 326 | 62 | 0.46 ¹ |
| S2 | 16 14 43.1 | -50 11 21 | 16148-5011 | 64.6 | 208 | 1822 | 2648 | 1357 | 766 | 52 | — |
| S3 | 16 15 01.1 | -50 16 02 | — | — | 140 | 1229 | 2253 | 648 | 308 | 32 | — |
| S4 | 16 15 23.3 | -50 16 27 | 16153-5016 | 103 | 140 | 1229 | 2253 | 690 | 342 | 38 | — |
| S5 | 16 15 31.2 | -50 45 08 | — | 52.5 | 143 | 1193 | 1432 | 653 | 338 | 32 | — |
| S6 | 16 15 34.6 | -50 01 46 | 16156-5002 | 102 | 359 | 2930 | 3492 | 2379 | 1275 | 82 | 1.0 ¹ |
| S7 | 16 15 42.1 | -50 56 25 | 16158-5055 | 331 | 1732 | 8140 | 8158 | 6373 | 3079 | 249 | 0.55 ¹ |
| S8 | 16 15 48.4 | -50 12 29 | 16159-5012 | 54.7 | 257 | 2611 | 3801 | 1910 | 976 | 71 | 0.17 ¹ |
| S9 | 16 15 58.6 | -50 07 53 | — | — | — | — | — | 1332 | 996 | 9.8 | — |
| S10 | 16 16 00.7 | -50 50 48 | 16159-5049 | 137 | 503 | 3200 | 3713 | 2050 | 817 | 91 | — |
| S11 | 16 16 18.2 | -50 46 08 | 16164-5046 | 221 | 2033 | 14120 | 16790 | 15380 | 7790 | 411 | 1.04 ¹ |
| S12 | 16 16 37.5 | -50 41 17 | — | — | — | — | — | 1073 | 512 | 21 | — |
| S13 | 16 16 43.3 | -50 29 09 | — | — | — | — | — | 2715 | 1275 | 56 | — |
| S14 | 16 16 58.2 | -50 52 56 | 16170-5053 | — | 203 | 1338 | 1485 | 582 | 333 | 31 | — |
| S15 | 16 17 10.8 | -50 27 48 | 16172-5028 | 468 | 3044 | 12920 | 18355 | 20811 | 10009 | 482 | 0.58 ¹ |
| S16 | 16 17 31.5 | -50 45 52 | 16175-5045 | — | 101 | 1141 | 1818 | 2372 | 1546 | 37 | — |
| S17 | 16 17 31.6 | -50 02 20 | 16175-5002 | 40.2 | 177 | 1833 | 3201 | 3198 | 2132 | 62 | 1.50 ^{2,3} |
| S18 | 16 17 33.3 | -50 22 37 | 16174-5022 | 134 | 600 | 4019 | 5576 | 2180 | 1043 | 115 | — |
| S19 | 16 17 42.9 | -50 34 03 | — | — | — | — | — | 973 | 1017 | 5.4 | — |
| S20 | 16 17 42.9 | -50 18 52 | 16177-5018 | 417 | 3164 | 13207 | 17243 | 15572 | 8015 | 460 | 0.72 ^{1,2} |
| S21 | 16 17 53.3 | -50 12 25 | — | — | — | 1088 | 2168 | 572 | 456 | 19 | — |
| S22 | 16 18 10.4 | -50 04 18 | — | 54.8 | 214 | 1970 | 3940 | 2194 | 1524 | 65 | — |
| S23 | 16 18 22.9 | -49 58 25 | 16183-4958 | 3372 | 12097 | 12395 | 16785 | 27841 | 11555 | 921 | >0.57 ^{1,2,3} |

* Units of Right Ascension are hours, minutes and seconds, and the units of Declination are degrees, minutes and seconds.

[†] Flux densities are within $3'$ diameter.

[‡] References of radio data for calculating IRE are – 1) Shaver & Goss (1970b); 2) Retallack & Goss (1980); 3) Forster et al. (1987).

chopped observations: $\leq 50\%$ for Carina complex (Ghosh et al. 1988), 35% for W 31 (Ghosh et al. 1989b) and 35% for *IRAS* 09002–4732 region (Ghosh et al. 2000) .

3.4 Comparison with radio observations

We have looked for association of the FIR sources with radio continuum sources detected by others, demanding that positions match within $2''.0$. We find 10 associations. Taking the FIR luminosity listed in Table 1 as that due to a single ZAMS star, we can estimate the expected rate of emission of Lyman continuum photons. We can also compute the same from the observed radio continuum flux density using the formula of Mezger (1978). We have used the 5000 MHz flux density given by Shaver & Goss (1970b) (at an angular resolution of $4'$) wherever available since at this high frequency the radio emission is less affected by optical depth effects. For source S17 we have used the mean of the 1415 MHz flux density of Retallack & Goss (1980) and 1420 MHz flux density of Forster et al. (1987) with an angular resolution $\sim 1'$. We have not used very high resolution ($\sim 1''$) interferometric radio observations of Walsh et al. (1998) as they only give peak flux densities. In Table 1 we present IRE, the ratio of Lyman continuum luminosity derived from the FIR and radio observations. If the

radio emission is optically thin and the source is powered by a single ZAMS star, $\text{IRE} = 1$. If however, the energizing source is multiple or if some fraction of Lyman continuum luminosity is absorbed by dust and not available for ionizing the gas, we expect $\text{IRE} > 1$. This can also result if a fraction of the FIR luminosity is due to accretion (Garay & Lizano 1999) since accretion is unlikely to produce energetic Lyman continuum photons. From Table 1 we find that only one source viz., S17 has IRE significantly higher than unity and even for this, it is consistent with unity if 50 % of Lyman continuum photons are unavailable for ionization because of dust absorption (Smith, Biermann & Mezger 1978). For all other sources the ratio is ≤ 1 ; this is most probably due to the fact that the resolution of radio observations used is generally much poorer than that of our FIR observations.

It is generally believed that massive stars are formed in clusters. We may, therefore, have additional unresolved stars within our effective resolution of $1''.2$. However, in the light of IRE discussed above, we cannot make definite statement about the presence of multiple sources. We can only conclude that another massive star with a significant fraction of observed luminosity is unlikely to be present. Similar statement can also be made for luminosity from accretion.

4 STELLAR LUMINOSITY DISTRIBUTION AND INITIAL MASS FUNCTION

For deeply embedded objects like the RCW 106, the FIR luminosity is almost the bolometric luminosity of the energizing star(s). Making use of the 23 objects detected by us, we construct the stellar luminosity distribution of massive stars in the RCW 106 complex. This is shown in Fig. 5. From an inspection of the figure we see that our sampling is nearly complete for $L > 20,000 L_{\odot}$. Assuming the luminosity distribution to be a power law given by $N[\log (L/L_{\odot})] \propto \alpha \log (L/L_{\odot})$ and using the more robust (as compared to binning) maximum likelihood method, we find $\alpha = -0.67 \pm 0.22$ for $L > 20,000 L_{\odot}$. It may be noted that due to factors discussed in the previous section, the observed distribution could be flatter than the intrinsic one. Our value of slope may be compared with the value of -0.56 derived by Rengarajan (1984) from the M17SW data of Jaffe, Stier & Fazio (1982).

The initial mass function (IMF) of stars is usually defined as the birth rate of stars formed per unit logarithmic mass interval per unit time. The shape of the IMF ($\xi(\log m_*)$) is generally characterized as a power law with a spectral index (β). The IMF at birth is normally

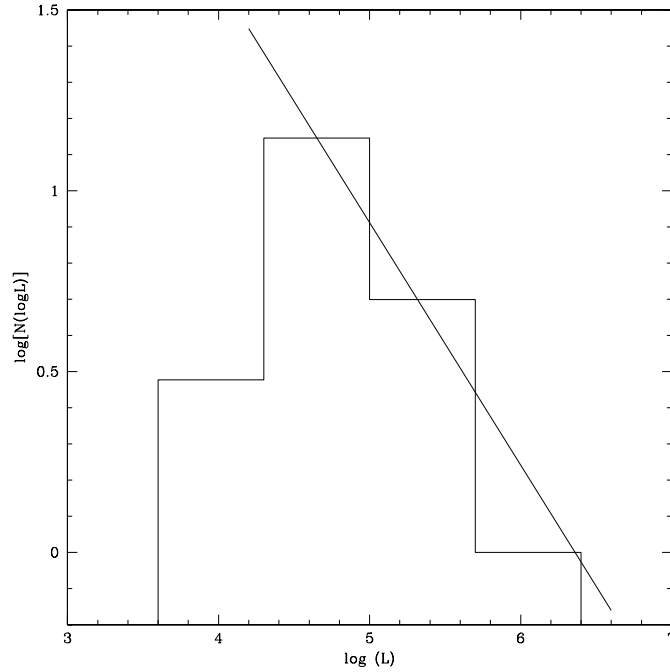


Figure 5. Luminosity distribution for sources in RCW 106 region. The line shows the fit obtained using maximum likelihood method assuming power law type of number distribution.

derived from the observed present day mass function (PDMF) and applying corrections to it. For example, the well known Salpeter IMF (Salpeter 1955) and Miller Scalo IMF (Miller & Scalo 1979) are derived from the population of field stars after correcting for life times, scale heights etc. These estimates are, therefore, averaged over a large volume and over the life of the Galaxy. In a recent review Scalo (1998) summarises the more accurate spectroscopic observations of massive stars in clusters and associations (age up to a few million years) and concludes that there is a large uncertainty in the value of β and that it ranges between -1 and -2 . An interesting question is what is the shape of IMF at a very early stage when stars are still deeply embedded in molecular clouds? The large number of high mass stars observed in the RCW complex and a young age ($< 100,000$ years) give us an opportunity to study the IMF at birth. For this purpose, the FIR luminosities were used to obtain masses using the mass–luminosity relation for a ZAMS star with solar metallicity, using the analytical relation given by Tout et al. (1996). Again using the maximum likelihood method we find $\beta = -1.73 \pm 0.5$ for mass $\geq 15 M_{\odot}$. As is the case for the luminosity distribution, the actual IMF would be steeper. This slope is in the same region as the values determined for massive stars and for stars of intermediate mass from photometric observations of stellar clusters (Scalo 1998). Ghosh et al. (2000) obtained $\beta = -1.25$ in the mass range of $4\text{--}16 M_{\odot}$ in the complex around *IRAS* 09002–4736. Okumura et al. (2000) using near infrared imaging

Table 2. Parameters* for the models shown in Figures 6 and 7

| Source | Best fit | | | | | Second best fit | | | | | | $\chi^2\dagger$ | Poorest fit | | | | | |
|--------|-----------|------------------------|----------|--------------|-----------|-----------------|------------------------|----------|--------------|-----------|-----------|-----------------|------------------------|----------|--------------|-----------|-----------------|--|
| | R (pc) | R _c (pc) | γ | τ_{100} | f_{sil} | R (pc) | R _c (pc) | γ | τ_{100} | f_{sil} | R (pc) | | R _c (pc) | γ | τ_{100} | f_{sil} | $\chi^2\dagger$ | |
| S2 | 0.64 | 0.017 | 1 | 0.19 | 0.13 | 0.68 | 0.009 | 0 | 0.06 | 0.66 | 1.0 | 0.60 | 0.064 | 2 | 0.17 | 0.10 | 4.7 | |
| S4 | 0.26 | 0.016 | 1 | 0.21 | 0.00 | 0.38 | 0.008 | 0 | 0.07 | 0.23 | 1.3 | 0.30 | 0.034 | 2 | 0.20 | 0.00 | 1.8 | |
| S5 | 0.37 | 0.006 | 0 | 0.07 | 0.39 | 0.39 | 0.018 | 1 | 0.16 | 0.16 | 1.4 | 0.38 | 0.040 | 2 | 0.16 | 0.10 | 2.9 | |
| S6 | 0.81 | 0.009 | 1 | 0.25 | 0.07 | 1.04 | 0.013 | 0 | 0.05 | 0.89 | 6.1 | 0.90 | 0.087 | 2 | 0.17 | 0.06 | 40.0 | |
| S7 | 2.14 | 0.038 | 1 | 0.10 | 0.33 | 1.22 | 0.028 | 0 | 0.06 | 0.56 | 5.4 | 1.10 | 0.153 | 2 | 0.12 | 0.05 | 6.8 | |
| S8 | 0.56 | 0.021 | 1 | 0.22 | 0.12 | 0.61 | 0.009 | 0 | 0.09 | 0.55 | 1.7 | 0.44 | 0.070 | 2 | 0.20 | 0.09 | 5.7 | |
| S10 | 0.58 | 0.021 | 0 | 0.07 | 0.45 | 0.87 | 0.026 | 1 | 0.11 | 0.28 | 1.5 | 0.56 | 0.009 | 2 | 0.13 | 0.14 | 3.7 | |
| S11 | 2.62 | 0.054 | 1 | 0.18 | 0.10 | 2.08 | 0.182 | 0 | 0.09 | 0.40 | 1.5 | 2.77 | 0.168 | 2 | 0.18 | 0.07 | 11.0 | |
| S15 | 4.36 | 0.051 | 1 | 0.15 | 0.20 | 2.42 | 0.017 | 0 | 0.08 | 0.47 | 7.6 | 2.13 | 0.219 | 2 | 0.13 | 0.06 | 11.0 | |
| S17 | 1.24 | 0.016 | 0 | 0.11 | 0.48 | 1.06 | 0.040 | 1 | 0.25 | 0.08 | 4.6 | 0.72 | 0.146 | 2 | 0.22 | 0.06 | 22.6 | |
| S18 | 0.69 | 0.022 | 1 | 0.15 | 0.18 | 0.69 | 0.016 | 0 | 0.06 | 0.75 | 1.2 | 0.50 | 0.093 | 2 | 0.14 | 0.95 | 1.8 | |
| S20 | 4.32 | 0.063 | 1 | 0.11 | 0.36 | 1.93 | 0.010 | 0 | 0.07 | 0.51 | 19.0 | 1.13 | 0.212 | 2 | 0.16 | 0.10 | 24.3 | |
| S22 | 0.78 | 0.024 | 1 | 0.27 | 0.06 | 0.84 | 0.014 | 0 | 0.10 | 0.47 | 1.3 | 1.76 | 0.083 | 2 | 0.22 | 0.03 | 12.2 | |

*For each source three sets of parameters are given. These are for the best fit models for each of the three types of density distributions. The order among the three sets is according to the fit. Thus the first set corresponds to the best fit out of the three, the last corresponds to the poorest fit. The parameters are – R, the radius of the cloud, R_c the radius of the central dust free cavity, γ , the power law index of the radial density distribution [$\rho(r) \propto r^{-\gamma}$], τ_{100} , the radial optical depth at 100 μm and f_{sil}, the fractional abundance of silicate.

$^\dagger \chi^2$ values are given relative to the best fit (i.e. $\chi^2_{\text{Second best fit}}/\chi^2_{\text{Best fit}}$ and $\chi^2_{\text{Poorest fit}}/\chi^2_{\text{Best fit}}$).

observations of W51 find that the slope above 10 M_☉ is consistent with -1.8 and perhaps flattens above 30 M_☉.

5 RADIATION TRANSFER MODELLING

5.1 Modelling Procedure

The emergent SED of an embedded source depends on the luminosity of the source and the physical properties of its dusty envelope. By fitting the observed SED to radiation transfer calculation, one can obtain useful information on the geometric details and nature of dust. With this in mind we have chosen, from Table 1, thirteen sources that have measured flux densities in all six bands, viz. , the two TIFR and four *IRAS* bands. The source S23 was excluded as the *IRAS* signals at 60 and 100 μm are saturated. The radiation transfer calculation was carried out through a purely dust component in a spherical geometry using the code CSDUST3 (Egan, Leung and Spagana 1988). The central source was assumed to be a single star with a luminosity equal to the value derived from observations. A mixture of graphite and astronomical silicate with properties as given by Laor & Draine (1993) was assumed. Size distribution $[n(a)]$ was assumed to be a power law $[n(a) \propto a^{-3.5}]$ as per Mathis et al. (1977). The free parameters of the model were – R, the size of the envelope , R_c, the size of the central dust free cavity , τ_{100} , the total (due to both type of grains) radial optical

Table 3. Density distribution near embedded high mass stars

| <i>Resolution</i> | γ | Reference |
|-------------------|----------|--|
| 1'2 | 0 or 1 | (FIR) Present work, Ghosh et al. (2000), Mookerjee et al. (1999,2000) |
| 0'5 | 0 or 1 | (FIR) (Campbell et al. 1995) |
| 0'15 | 0 | (MIR) (Faison et al. 1998) |
| 0'15/0'25 | 1.5 | (Sub-mm) (Hatchell et al. 2000) |
| 0'5 | 2–1 | (Sub-mm) (Hunter 1997) |

depth at $100 \mu\text{m}$, f_{sil} , the fractional abundance of silicate and γ , the power law index of the radial density distribution within the envelope [$\rho(r) \propto r^{-\gamma}$]. Only three discrete values of 0, 1 and 2 were explored for γ . A χ^2 minimization scheme was developed for fitting the computed SED of the model to the observed SED of the source and the fitting was done for each value of γ .

The sensitivity of the χ^2 minimization scheme in terms of extracting the parameters (mainly for index γ) accurately from the input observed SED of the source was tested using simulation. Synthetic input was created by calculating the flux densities at the six wavelengths used as well as in the NIR ($5 \mu\text{m}$) and sub-mm ($800 \mu\text{m}$) with added random noises. From the results of the simulation we conclude that i) the best fit always corresponds to the case when the γ value is the same for the input spectrum and the modelled spectrum; presence of NIR point improves the discrimination especially for $\gamma = 1$ or 2; ii) the radius of the central dust free cavity and optical depth at $100 \mu\text{m}$ are the most sensitive parameters of the modelling procedure, the variation between the input parameters and the extracted parameters for both is about 20%, while for the outer radius it is about 30%; iii) the dust composition is a parameter with poor extraction accuracy since the absorption efficiency beyond about $50 \mu\text{m}$ is the same for graphite and silicate and the main constraints come from data points at $25 \mu\text{m}$ or lower.

5.2 Results of modelling RCW 106 sources

Figures 6 and 7 show the observed data points and the best fit SED for each value of γ for the 13 selected sources. The parameters of these models, along with relative χ^2 values, are presented in Table 2.

From Figs. 6, Fig. 7 and Table 2 it is seen that for 9 out of the 13 sources r^{-1} distribution fits the SED best while for the rest, uniform distribution is the best fit. It may be mentioned

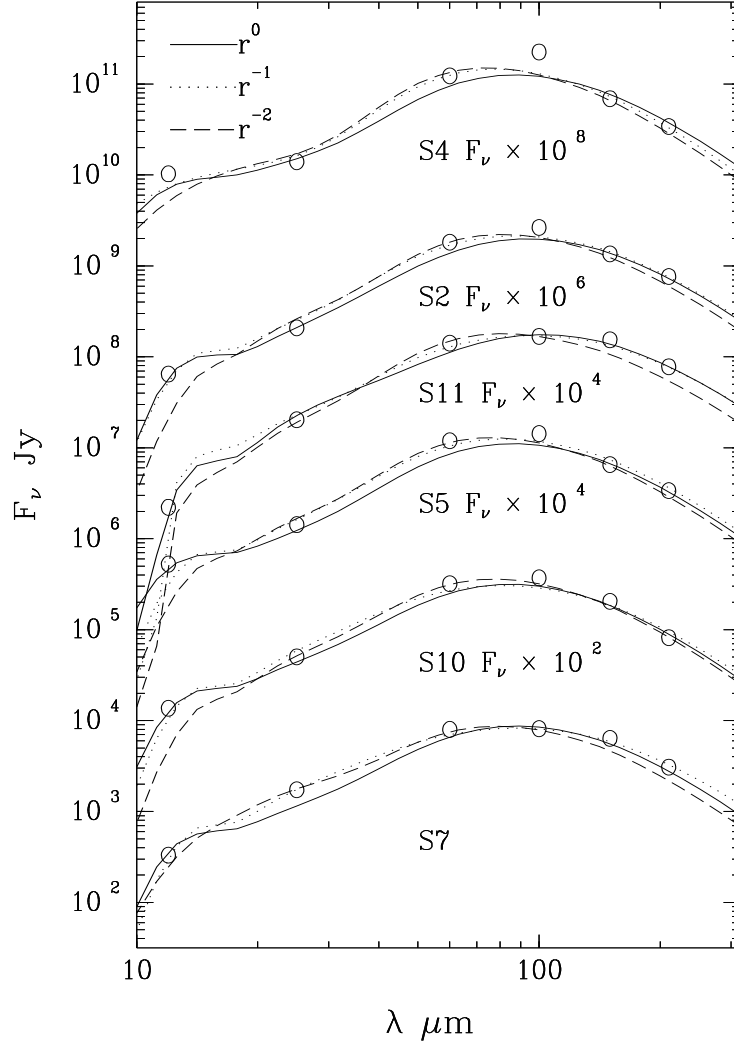


Figure 6. Spectral energy distribution for the six sources S7, S10, S5, S11, S2 and S4 in RCW 106 complex region as given in Table 1. The lines shown are fits from radiation transfer models. Different lines depict fits for three different power law dependence of radial density. The parameters for these fits are given in Table 2. Note that for the sake of clarity flux densities have been multiplied by a different constant factor for five of the sources.

that there is not much difference between the the final χ^2 obtained for the best fits for the two density distributions. The r^{-2} distribution shows the poorest fit for all sources. Table 3 lists the radial distribution index obtained in recent times by different authors using radiation transfer modelling of envelopes of high mass embedded sources. This compilation suggests that in many cases the density distribution differs from $\rho(r) \propto r^{-2}$ or $r^{-1.5}$ that is expected for the envelopes of young protostars (Shu, Adams & Lizano 1987). Is there really a lack of sources with r^{-2} density distribution as revealed by FIR and MIR observations? This can be checked only through higher angular resolution observations at FIR wavelengths and modelling actual radial intensity profiles. However, there is no prospect of large improvement of angular resolution in the FIR in the near future. If the density distribution is indeed

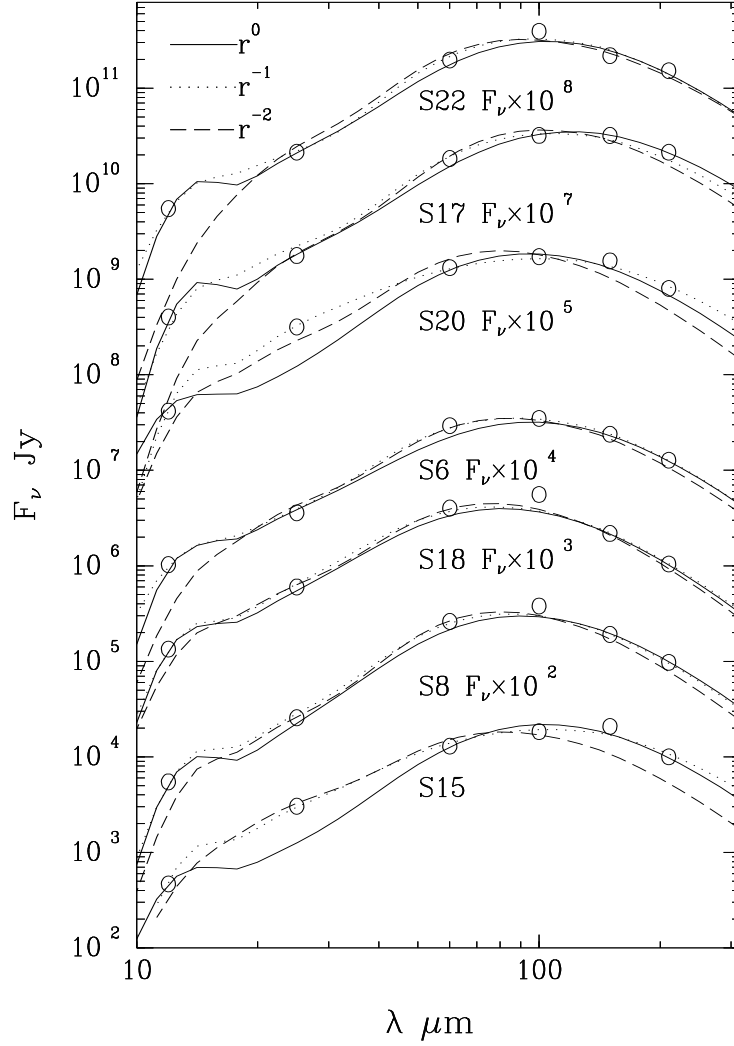


Figure 7. SED plots similar to those in Fig. 6, but for sources S15, S8, S18, S6, S20, S17 and S22.

different from that expected for free fall models (i.e. $\propto r^{-2}$), what are the possible reasons for this? Do high velocity outflows arising from young high mass stars and radiation pressure on dust grains due to intense UV radiation from the young high mass star help in modifying the initial free fall density distribution $\propto r^{-2}$? Jijina & Adams (1996), accounting for effect of radiation pressure, predict that close to the star, density distribution should be $\propto r^{-0.5}$ and at larger distances $\propto r^{-1.5}$. One should note that these solutions are at much smaller scales compared to those sampled by the large beams of most of the FIR observations.

5.3 Luminosity and Envelope Mass

The mass computed from the best fit model parameters represents the mass of the star forming envelope if one assumes a constant gas to dust ratio. In Fig. 8 the luminosity of

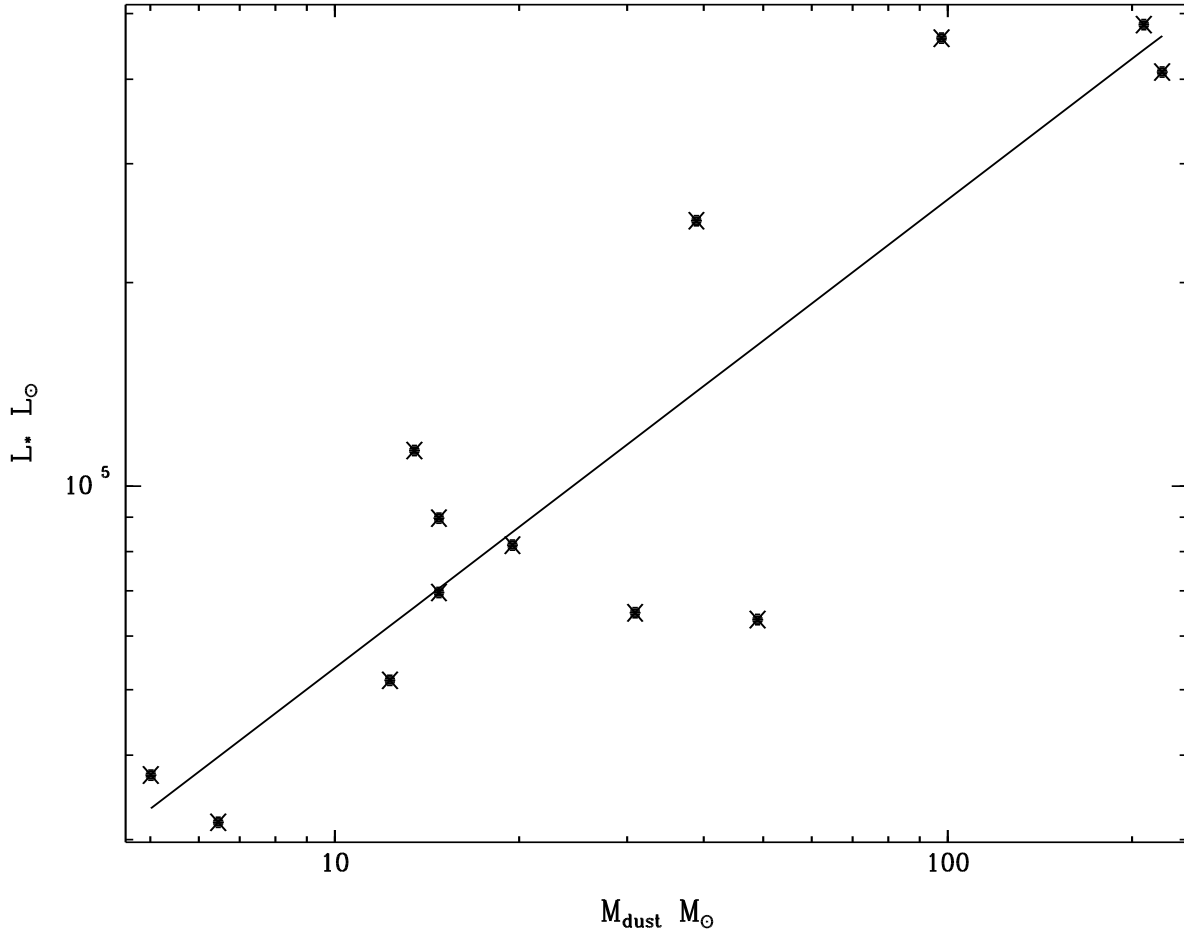


Figure 8. The FIR luminosity of the source plotted against the mass of the dust envelope obtained from the best fit radiation transfer model. The solid line represents the power law regression fit to the points.

the source is plotted against the computed dust mass of the envelope. A correlation is seen between the two. The probability of finding no correlation is as low as 0.0086. The power law index after regression analysis is found to be 0.7 ± 0.11 . This indicates that the more massive molecular cores produce more massive stars.

6 SUMMARY

The star forming region associated with RCW 106 has been mapped simultaneously at 150 and 210 μm . The HIRES processed *IRAS* survey data are used as supplement to our data. The temperature and the FIR optical depth maps have been generated for the region. The total dust mass estimated from the optical depth map is about 1800 M_\odot . The local maxima in the 210 μm map have been searched for to find the embedded sources. The associations of these sources are found in the four *IRAS* maps and the 150 μm map. The diffuse fraction

in these maps is found to be 81% and 84% in the *IRAS* 60 and 100 μm bands while it is 19% and 27% at 150 and 210 μm from our chopped observations. The SEDs for the sources are constructed and FIR luminosities estimated. Luminosity distribution of these sources has been obtained. These FIR luminosities are used, along with mass-luminosity relation for ZAMS stars, to obtain IMF of the region. The estimated power law index of IMF is -1.73 for mass $\geq 15 M_{\odot}$ similar to that of other star forming regions and OB associations albeit flatter than the IMF for field stars. The SEDs of the sources detected in all the bands are modelled using radiation transfer calculations assuming a dusty envelope surrounding the young ZAMS star with luminosity equal to that of the FIR luminosity of the source. The size of the envelope, inner dust free core radius, line of sight optical depth due to dust at 100 μm and composition of the dust were varied to obtain the best fit to the observed SED. Three types of radial density distributions – $[\rho(r) \propto r^{-n}$ where $\gamma=0, 1$ and 2] were tried for. The best fit results show that r^{-2} can be ruled out against uniform and r^{-1} distributions. A correlation was found between the the source luminosity and the mass of dusty envelopes calculated using the best fit model parameters.

Acknowledgements

We thank S.L. D’Costa, M.V. Naik, S.V. Gollapudi, D.M. Patkar, M.B. Naik and G.S. Meshram for their support for the experiment. The members of TIFR Balloon Facility (Balloon group and Control & Instrumentation group), Hyderabad, are thanked for their roles in conducting the balloon flights. IPAC is thanked for providing HIRES processed *IRAS* data. TNR thanks JSPS and Dr. H. Shibai for the Invitation Fellowship at the Physics Department, Nagoya University where part of this work was done.

REFERENCES

- Aumann H. H., Fowler J. W., Melnyk M., 1990, *AJ*, 99, 1674
- Batchelor R. A., Caswell J. L., Haynes R. F., Wellington K. J., Goss W. M., Knowles S. H., 1980, *Australian Journal of Physics*, 33, 139
- Batchelor R. A., Gardner F. F., Knowles S. H., Mebold U., 1977, *Proceedings of the Astronomical Society of Australia*, 3, 152
- Braz M. A., Gregorio Hetem J. C., Scalise J. E., Monteiro Do Vale J. L., Gaylard M., 1989, *A&AS*, 77, 465
- Braz M. A., Scalise J. E., 1982, *A&A*, 107, 272
- Campbell M. F., Bunter H. M., Harvey P. M., Evans II N. J., Campbell M. B., Sabbey C. N., 1995, *ApJ*, 454, 831
- Caswell J. L., Haynes R. F., 1975, *MNRAS*, 173, 649
- Caswell J. L., Haynes R. F., Goss W. M., 1980, *Australian Journal of Physics*, 33, 639
- Caswell J. L., Vaile R. A., Ellingsen S. P., Norris R. P., 1995, *MNRAS*, 274, 1126
- Egan M. P., Leung C. M., Spagana G. F., 1988, *Computer Physics Communications*, 48, 271
- Ellingsen S. P., Von Bibra M. L., McCulloch P. M., Norris R. P., Deshpande A. A., Phillips C. J., 1996, *MNRAS*, 280, 378

- Faison M., Churchwell E., Hofner P., Hackwell J., Lynch D. K., Russel R. W., 1998, *ApJ*, 500, 280
- Forster J. R., Whiteoak J. B., Kesteven M. J., Manchester R. N., Rayner P. T., Ables J. G., Peters W. L., 1987, *MNRAS*, 226, 173
- Gardner F. F., Whiteoak J. B., 1978, *MNRAS*, 183, 711
- Gardner F. F., Whiteoak J. B., 1984, *MNRAS*, 210, 23
- Garay G., Lizano S., 1999, *PASP*, 111, 1049
- Ghosh S. K., Iyengar K. V. K., Rengarajan T. N., Tandon S. N., Verma R. P., Daniel R. R., 1988, *ApJ*, 330, 928
- Ghosh S. K., Iyengar K. V. K., Rengarajan T. N., Tandon S. N., Verma R. P., Daniel R. R., 1989a, *ApJS*, 69, 233
- Ghosh S. K., Iyengar K. V. K., Rengarajan T. N., Tandon S. N., Verma R. P., Daniel R. R., Ho P. T. P., 1989b, *ApJ*, 347, 338
- Ghosh S. K., Iyengar K. V. K., Rengarajan T. N., Tandon S. N., Verma R. P., Daniel R. R., 1990, *ApJ*, 353, 564
- Ghosh S. K., Mookerjee B., Rengarajan T. N., Tandon S. N., Verma R. P., 2000, *A&A*, 363, 744
- Gillespie A. R., Huggins P. J., Sollner T. C. L. G., Phillips T. G., Gardner F. F., Knowles S. H., 1977, *A&A*, 60, 221
- Goss W. M., Shaver P. A., 1970, *Aust. J. Phys. Astrophys. Suppl.*, No. 14, 1
- Hatchell J., Fuller G. A., Miller T. J., Thompson M. A., Macdonald G. H., 2000, *A&A*, 357, 637
- Hildebrand H., 1983, *QJRAS*, 24, 267
- Hunter T. R., 1997, Ph.D. thesis, California Institute of Technology
- Jaffe D. T., Stier M. T., Fazio G. G., 1982, *ApJ*, 252, 601
- Jarrett T. H., Dickman R. L., Herbst W., 1989, *ApJ*, 345, 881
- Jijina J., Adams F. C., 1996, *ApJ*, 462, 874
- Karnik A.D., 2000, Infrared observations of star forming regions, Ph D thesis, University of Bombay, Bombay
- Kaufmann P., Scalise J. E., Schaal R. E., Gammon R. H., Zisk S., 1977, *AJ*, 82, 577
- Langer W. D., Wilson R. W., Goldsmith P. F., Beichman C. A., 1989, *ApJ*, 337, 355
- Laor A., Draine B. T., 1993, *ApJ*, 402, 441
- Lockman F. J., 1979, *ApJ*, 232, 761
- Macleod G. C., Gaylard M. J., 1992, *MNRAS*, 256, 519
- Macleod G. C., van der Walt D. J., North A., Gaylard M. J., Galt J. A., Moriarty-Schieven G. H., 1998, *AJ*, 116, 2936
- Mathis J. S., Ruml W., Nordsieck K. H., 1977, *ApJ*, 217, 425
- Mezger P. G., 1978, *A&A*, 70, 565
- Miller G. E., Scalzo J. M., 1979, *ApJS*, 41, 513
- Mookerjee B., Ghosh S.K., Karnik A.D., Rengarajan T.N., Tandon S.N., Verma R.P., 1999, *ApJ*, 522, 285
- Mookerjee B., Ghosh S.K., Rengarajan T.N., Tandon S.N., Verma R.P., 2000, *ApJ*, 539, 775
- Naik M.V., D'Costa S.L., Ghosh S.K., Mookerjee B., Ojha D.K., Verma R.P., 2000, *PASP*, 112, 273
- Okumura S., Mori A., Nishihara E., Watanabe E., Yamashita T., 2000, *ApJ*, 543, 799
- Rengarajan T. N., 1984, *ApJ*, 287, 671
- Retallack D. S., Goss W. M., 1980, *MNRAS*, 193, 261
- Rodgers A. W., Campbell C. T., Whiteoak J. B., 1960, *MNRAS*, 121, 103
- Salpeter E. E., 1955, *ApJ*, 121, 161
- Scalise J., E., Rodriguez L. F., Mendoza-Torres E., 1989, *A&A*, 221, 105
- Scalo J. M., 1998, in *Stellar Initial Mass Function*, ASP Conference Series, Vol. 142, 201
- Schutte A. J., van der Walt D. J., Gaylard M. J., Macleod G. C., 1993, *MNRAS*, 261, 783
- Shaver P. A., Goss W. M., 1970a, *Aust. J. Phys. Astrophys. Suppl.*, No. 14, 77
- Shaver P. A., Goss W. M., 1970b, *Aust. J. Phys. Astrophys. Suppl.*, No. 14, 133
- Shu F. H., Adams F. C., Lizano S., 1987, *ARAA*, 25, 23
- Smith L. F., Biermann P., Mezger P.G., 1978, *A&A*, 66, 65
- Tout C. A., Poles O. R., Eggleton P. P., Han Z., 1996, *MNRAS*, 281, 257

- van der Walt D. J., Gaylard M. J., Macleod G. C., 1995, *A&AS*, 110, 81
- van der Walt D. J., Retief S. J. P., Gaylard M. J., Macleod, G. C., 1996, *MNRAS*, 282, 1085
- Verma R. P., Bisht R. S., Ghosh S. K., Iyengar K. V. K., Rengarajan T. N., Tandon S. N., 1994, *A&A*, 284, 936
- Verma R. P., Rengarajan T. N., Ghosh S. K., 1993, *Bulletin of the Astronomical Society of India*, 21, 489
- Walsh A. J., Burton M. G., Hyland A. R., Robinson G., 1998, *MNRAS*, 301, 640